Nomoto et al. *NPG Asia Materials* (2022) 14:76
https://doi.org/10.1038/s41427-022-00421-4

NPG Asia Materials

ARTICLE Open Access

Over 130 cm^2/Vs Hall mobility of flexible transparent conductive In_2O_3 films by excimer-laser solid-phase crystallization

Junichi Nomoto[1], Takashi Koida[2], Iwao Yamaguchi[1], Hisao Makino[3], Yuuki Kitanaka[1], Tomohiko Nakajima[1] and Tetsuo Tsuchiya[1]

Abstract

Flexible transparent electrodes on flexible plastic sheets are in significant demand for use in flexible perovskite solar cells (*f*-PSCs). However, the combination of the broadband high optical transparency and low electrical resistivity required for the tandemization of *f*-PSCs sets a stringent requirement on flexible transparent electrodes that are based on traditional Sn-doped In_2O_3 (ITO) films, owing to the high free-carrier concentration needed to reduce the electrical resistivity. Herein, we used excimer laser irradiation to achieve a Ce and H codoped In_2O_3 (ICO:H) film on flexible polyethylene terephthalate (PET) that had ultrahigh electron mobility of 133 cm^2/Vs, which is the highest among those reported for flexible transparent electrodes, and low sheet resistance of 14.2 Ω/□, which is approximately three times lower than the 40 Ω/□ sheet resistance of commercially available ITO/PET. Furthermore, compared to ITO, this ICO:H film had higher infrared transparency. These nontrivial performances were achieved by an optimized excimer-laser solid-phase crystallization process guided by the correlation between laser pulse counts and the volume fractions of the amorphous and crystalline phases in the films. These high performances resolved the problems faced by ITO films, thus facilitating the performance of flexible solar cells and optoelectronic devices.

Introduction

Transparent conducting oxide (TCO) films have been widely used as transparent electrodes in optoelectronic applications, such as displays, light-emitting diodes, solar cells, and other optoelectronic devices[1–4]. In recent years, flexible transparent electrodes on flexible plastics, such as polyethylene terephthalate (PET), polyethylene naphthalate (PEN), and polyimide, have been in significant demand for use in flexible perovskite solar cells (*f*-PSCs)[5–9]. Among all solar cells, *f*-PSCs produce the most competitive power-per-weight and thus are specifically attractive for applications in wearable, portable electronic devices, building-integrated photovoltaics, and drones. State-of-the-art *f*-PSCs can reach an efficiency of 19.51%[10]. A promising method for further increasing *f*-PSC efficiency is to construct tandem structures[11]. For example, the integration of a wide-bandgap (near-infrared (NIR)-transparent) perovskite front cell and a narrow-bandgap perovskite or $Cu(In,Ga)Se_2$ (CIGS) rear cell allowed a more efficient utilization of solar light with different photon energies[12–15].

Historically, magnetron-sputtered Sn-doped In_2O_3 (ITO) has been widely used as a TCO material[1–4,9]. However, using ITO films as transparent electrodes in *f*-PSCs with tandem structures limits the device performance. Due to the difficulty in achieving high carrier mobility (μ) by Sn doping, a high carrier concentration (N) by heavy Sn doping is necessary to reduce electrical resistivity (ρ)[9]. However, such doping usually results in

Correspondence: Junichi Nomoto (nomoto.junichi@aist.go.jp)
[1]Advanced Manufacturing Research Institute, National Institute of Advanced Industrial Science and Technology (AIST), 1-1-1, Higashi, Tsukuba, Ibaraki 305-8565, Japan
[2]Research Institute for Energy Conservation, National Institute of Advanced Industrial Science and Technology (AIST), 1-1-1, Umezono, Tsukuba, Ibaraki 305-8568, Japan
Full list of author information is available at the end of the article.

high optical losses in the NIR wavelength region due to reflectance and/or absorption attributed to free-carrier electrons[16,17]. This optical loss induces a total photocurrent loss of several mA/cm^2 for perovskite tandem structures[18]. Therefore, the successful fabrication of *f*-PSCs with tandem structures requires high-μ TCO films (because a high μ results in a low ρ at a low N) to thus provide high transparency with alleviated parasitic optical losses in the visible and NIR regions.

Conventional polycrystalline ITO films exhibit a low μ of 40 cm^2/Vs[19], whereas In_2O_3-ZnO (IZO) films with amorphous structures exhibit a μ of 60 cm^2/Vs[20,21]. In contrast, solid-phase crystallized H-doped In_2O_3 (*spc*-IO:H) thin films[22,23] and *spc*-Ce and H codoped In_2O_3 (*spc*-ICO:H)[24,25] thin films achieve very high μ values of over 100 cm^2/Vs and suitable low-N values ranging from 1×10^{20} to 2×10^{20} cm^{-3}, leading to low optical losses over a wide optical range[22–25]. These excellent optoelectronic properties have been demonstrated in high-efficiency rigid solar cells, such as silicon heterojunctions[22,26–28], CIGS[29–31], and perovskite-based tandem solar cells[32–37]. However, these attractive films (*spc*-IO:H and *spc*-ICO:H) have never been adopted in flexible solar cells because they have a fabrication-temperature issue, namely, a high-temperature annealing process for solid-phase crystallization is necessary to obtain the high μ that is an attractive feature of H and/or Ce dopants. Both *spc*-IO:H and *spc*-ICO:H films are fabricated by a two-step process. In the first step, amorphous precursor films are deposited on a substrate without intentional heating or at low temperature (100 °C) via ion plating with direct current arc discharge[24,25] (i.e., reactive plasma deposition (RPD)[38]), magnetron sputtering[22,23], or atomic layer deposition[31,39]. During deposition, water is introduced into the deposition chamber to induce the formation of an amorphous structure. In the second step, either thermal annealing at a temperature higher than 150–200 °C or flash lamp annealing[40] is performed to induce *spc* (solid-phase crystallization) and to achieve a high μ. Such a high processing temperature, however, limits the formation and adoption of these films on heat-sensitive flexible substrates such as PET, whose process temperature is less than 70–110 °C[7].

To resolve this temperature issue, we used an excimer laser irradiation (ELI) technique. Excimer lasers have high photon energies. For example, KrF (wavelength $\lambda = 248$ nm) excimer lasers can achieve photon energy of 5 eV, which should be sufficient to induce a photothermal reaction for crystallization[41–43]. Photothermal effects are achieved when the maximum temperature inside the film exceeds 400 °C; the temperature then decays over several hundreds of nanoseconds[44,45]. The temperature inside the film exceeds the crystallization temperature, but only during a very short irradiation time, and therefore thermal damage to the underlayer can be avoided. As a result, because high temperature is no longer a requirement for the fabrication of *spc*-ICO:H films, these films can be adopted in flexible solar cells, with the expectation of a significant improvement in conversion efficiency. As a proof of concept (Fig. 1), we fabricated an *spc*-ICO:H film on a flexible PET sheet by using ELI. In this work, we successfully obtained the highest μ of 133 cm^2/Vs among reported flexible TCO films and obtained a low sheet resistance (R_s) of 14.2 Ω/□ ($\rho = 2.13 \times 10^{-4}$ Ωcm) with a high average optical transmittance (T_{av}) of 83.7% in the visible to NIR region ($\lambda = 400$–2100 nm). This successful R_s value is much lower than that of commercially available flexible 150-nm-thick ITO/PET sheets (R_s of 40 Ω/□, and T_{av} of 74.3%). The demonstrated high performance of a flexible *spc*-ICO:H film and its low fabrication-temperature process have resolved the problems encountered by conventional flexible ITO films. Flexible *spc*-ICO:H films are therefore potential components for flexible optoelectronics, thus facilitating the performance of flexible solar cells and optoelectronic devices.

Results

Texture evolution

First, the relationship between the crystallization temperature of ICO:H films and the heat resistance of a PET sheet needs to be addressed. The as-deposited ICO:H film that formed on a glass substrate under the same deposition conditions as on the PET sheet started crystallization at approximately 190 °C, which was confirmed by in situ X-ray diffraction measurements. At that temperature, the film on the PET sheet was significantly deformed. This demonstrates the difficulty in achieving the crystallization of an ICO:H/PET sheet without heat damage to the PET sheet by conventional heat treatment.

The main result of our study is the crystallization process under ELI. Figure 2a shows plan-view SIM (scanning ion microscope) images of ICO:H under various laser pulse counts (PC) for ELI. Due to the purely amorphous-phase formation, the nonlaser-irradiated (as-deposited) ICO:H film exhibited featureless structures with smooth surfaces. This observation is consistent with the absence of crystalline peaks in the X-ray diffraction patterns of the films (not shown here). At $PC = 2500$ shots, crystal nucleation occurred, and numerous small grains (300 nm) were observed on the ICO:H film surface. At $PC = 5000$ shots, the film had a structure with embedded larger crystalline grains (870 nm) together with small grains (300 nm) in the amorphous matrix. At $PC > 5000$ shots, grain growth proceeded. The grain density for a film with $PC = 12{,}500$ shots was much higher than that with $PC = 10{,}000$ shots. At $PC = 15{,}000$ shots, the crystallization of the film was complete, and the film

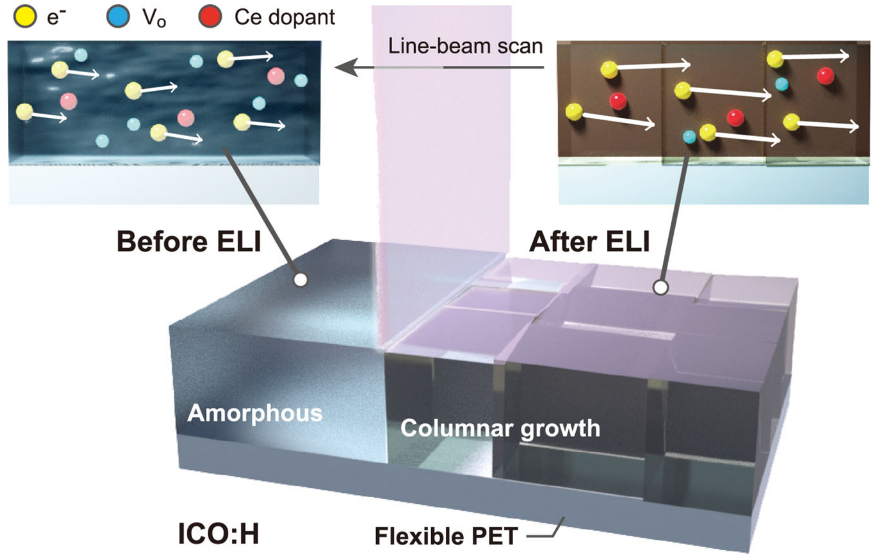

Fig. 1 Three-dimensional schematic diagram of carrier transport for the ICO:H films before (amorphous) and after (polycrystalline) excimer laser irradiation (ELI). Here, the carrier mobility μ depends on the relaxation time (τ) and electron effective mass (m) as $\mu = \tau/m$. The *spc*-ICO:H films exhibited an m similar to that of conventional polycrystalline ITO films, indicating that high μ is achieved via a larger τ rather than a smaller m[23,25]. Two origins are responsible for the large τ (= high μ) obtained for the *spc*-ICO:H films. One is that the Ce dopant can be suppressed to promote the formation of oxygen vacancies. These vacancies act as doubly charged donors, $V_O^{\bullet\bullet}$ (i.e., ionized impurity scattering centers), because Ce has larger binding energy with oxygen than does the In atom with Sn dopant (case of ITO). Another origin is that hydrogen can be passivated for the grain boundary states, thus leading to lower trap densities, which would consequently decrease the potential barriers at grain boundaries for electron transport[23,25].

exhibited a surface covered with large grains (>2 µm). At *PC* > 15,000 shots, crystallization did not continue, and the texture at *PC* = 30,000 shots was similar to that at 15,000 shots.

To obtain a better understanding of the crystallization process under ELI, we quantitatively determined the texture evolution by using electron backscatter diffraction (EBSD) measurements. Figure 2b shows inverse pole figure (IPF) maps along the normal direction for ICO:H films with *PC* = 2500, 5000, 10,000, and 15,000 shots. These IPF maps reveal that with increasing *PC*, the black area corresponding to the amorphous phase decreased due to the increase in the crystalized area. Figure 2c shows the grain size distribution, namely, the number of grains as a function of the grain size diameter. Figure 2d, e summarize the total number and area of grains, respectively, as a function of *PC*. At *PC* = 2500 shots, the grain size was small (0.1 to 0.6 µm in diameter), and the number of grains was low (157 grains); thus, the ratio of grains occupying the evaluation area (i.e., crystallized area) was ~5.1%. Taking into account that the adhesion of water molecules at growing surfaces suppresses the growth of crystallites[23], crystallite nuclei might have been created at the film surface due to the desorption of water molecules caused by a rapid rise in the temperature at the film surface region during the early stages of irradiation, i.e., when *PC* ≤2500 shots. At 5000 shots, the number of grains rapidly increased to 1035 grains, and the grain size increased to a maximum diameter of 1.5 µm. Therefore, the crystallized area was ~74%. These changes might be due to nucleation and grain growth. With a further increase in *PC* to 15,000 shots, the maximum grain size increased from 1.5 to 2.4 µm. Furthermore, the number of small grains (0.1–0.6 µm) decreased, whereas that of large grains (>1.2 µm) increased. Note that with this increase in *PC*, the total number of grains decreased to 593 grains, whereas the crystallized area increased to 99.7%. These data reveal that the grain growth during the increase in *PC* from 5000 to 15,000 shots was mainly caused by coalescence among grains. If two grains coalesce, they should form a grain boundary because the two grains typically have different orientations. However, no grain boundaries were identified within a single domain in the IPF maps in our study (Fig. 2b). This means that the orientation of the captured grains was transformed to that of the capturing grains. Figure 2f shows the pole figures (PFs) of the 111 reflections obtained from the IPF maps (Fig. 2b). In these PFs, the distribution of the poles for the 111 reflections appears as a spot in the center of the figure together with a ring. These results are evidence that most of the grains in the ICO:H film had a texture with a slight orientation in the <111> direction normal to the surface. This slight orientation might be caused by the (111) surface energy being the lowest among the low-indexed

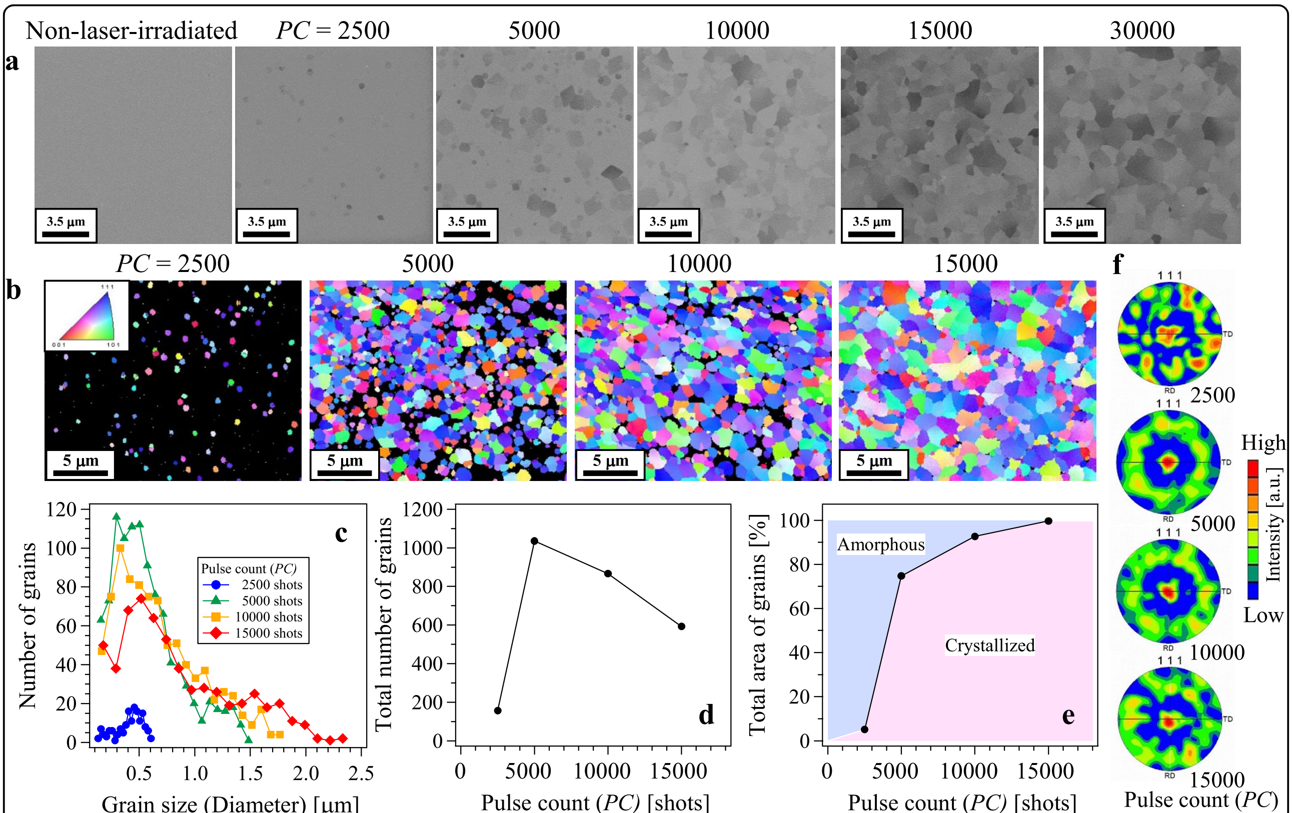

Fig. 2 Texture evolution of ICO:H films under ELI. a Plan-view SIM images of ICO:H films with various laser pulse counts (*PCs*). EBSD analysis data: **b** IPF maps along the normal direction of ICO:H films with *PC* = 2500, 5000, 10,000, and 15,000 shots; **c** Number of grains as a function of grain size (diameter); **d** Total number of grains; and **e** Total area of grains as a function of *PC*. **f** PFs of the 111 reflections.

surfaces in In_2O_3, including the (100), (110), and (111) surfaces[46].

Electrical and optical properties

In particular, this anomalous grain growth is very effective for enhancing the carrier transport properties. Figure 3a and Table 1 summarize the electrical properties of the ICO:H film under various *PCs* with ELI. Commercially available magnetron-sputtered 150-nm-thick ITO/PET sheets were used for comparison. At *PC* = 2500 shots, the ICO:H film showed a decrease in N from 2.72×10^{20} to $2.12 \times 10^{20}\ \mathrm{cm^{-3}}$ while showing a slight increase in Hall mobility (μ_H) from 43.3 to 45.6 $\mathrm{cm^2/Vs}$. At *PC* > 5000 shots, the ICO:H film showed a large increase in μ_H (decreases in R_s and ρ) with increasing *PC*. This change in μ_H was mainly caused by the texture change from the amorphous phase to the polycrystalline phase (discussed in the Texture evolution section above). N remained relatively constant, suggesting that the changes in R_s and ρ after ELI were governed by μ_H. At *PC* = 30,000 shots, the fully crystalized ICO:H film, therefore, achieved a high μ_H of 126 $\mathrm{cm^2/Vs}$, and thereby achieved a low R_s (ρ) of 17.2 Ω/□ (2.59×10^{-4} Ωcm). Furthermore, the ICO:H film under thermal-assisted ELI (i.e., low-temperature heating at 100 °C) achieved an ultrahigh μ_H of 133 $\mathrm{cm^2/Vs}$, and thereby a very low R_s (ρ) of 14.2 Ω/□ (2.13×10^{-4} Ωcm). To the best of our knowledge, these successful μ_H values are the highest among those reported for TCO/PET flexible sheets, as summarized in Table 2. This successful R_s value of 14.2 Ω/□ is much lower than that of commercially available 150-nm-thick ITO/PET sheets (~40 Ω/□).

Figure 3b compares the optical transmittance (T) and reflectance (R) spectra of a nonlaser-irradiated ICO:H film (hereafter denoted as an *a*-ICO:H film) and a fully crystalized ICO:H film with *PC* = 15,000 shots (hereafter denoted as an ELI-*spc*-ICO:H film). Additionally, the T and R spectra of ITO film with the same layer structure as the ICO:H film are shown. High transparency was measured across the visible and NIR range for the ELI-*spc*-ICO:H/SiO_2/PET and then compared with that for the ITO/SiO_2/PET. The average T (T_{av}) in the λ range from 400 to 2100 nm for the ELI-*spc*-ICO:H/SiO_2/PET was 83.7%, whereas that for the ITO/SiO_2/PET was 74.3%. This higher T_{av} was mainly caused by

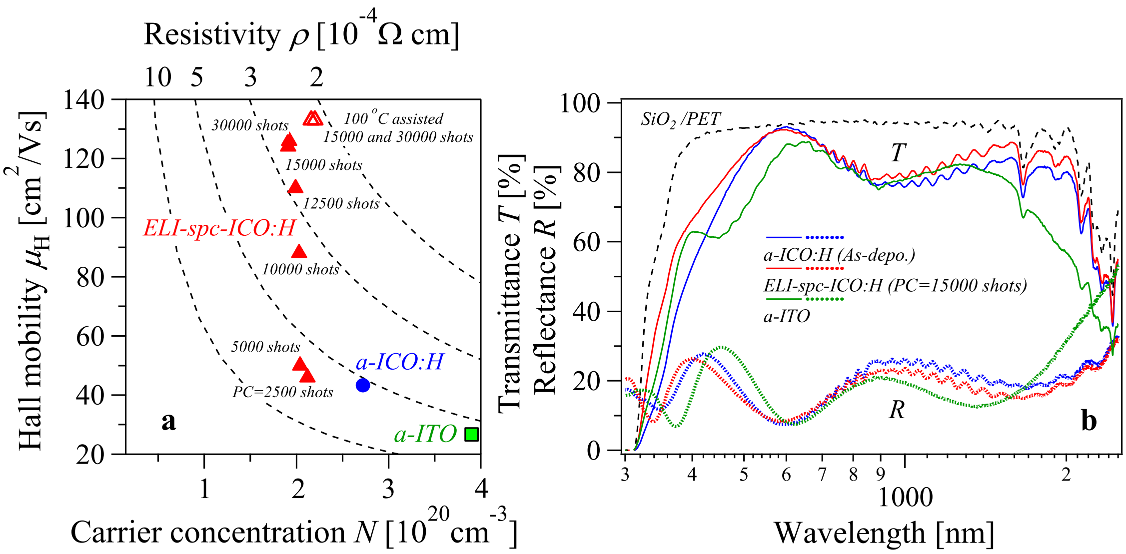

Fig. 3 Electrical and optical performance of ICO:H films. a ELI pulse count (*PC*) effect on the carrier concentration (*N*) and Hall mobility (μ_H) of ICO:H films. **b** Optical transmittance (*T*) and reflectance (*R*) spectra of the *a*-ICO:H film (nonlaser-irradiated) and fully crystalized ELI-*spc*-ICO:H film ($PC = 15{,}000$ shots).

Table 1 Electrical performance of ICO:H films.

Pulse count (*PC*) [shots]	Assisted temperature	Sheet resistance (R_s) [Ω/□]	Electrical resistivity (*ρ*) [Ωcm]	Carrier concentration (*N*) [cm^{-3}]	Hall mobility (μ_H) [cm^2/Vs]
0 (non-irradiated)	Unheated	35.4	5.31×10^{-4}	2.72×10^{20}	43.3
2500		42.9	6.44×10^{-4}	2.12×10^{20}	45.6
5000		41.0	6.15×10^{-4}	2.04×10^{20}	49.6
10,000		23.2	3.49×10^{-4}	2.03×10^{20}	88.2
12,500		19.0	2.84×10^{-4}	1.99×10^{20}	110
15,000	Unheated	17.5	2.63×10^{-4}	1.91×10^{20}	124
	100 °C	14.5	2.18×10^{-4}	2.16×10^{20}	133
30,000	Unheated	17.2	2.59×10^{-4}	1.92×10^{20}	126
	100 °C	14.2	2.13×10^{-4}	2.20×10^{20}	133

Sheet resistance (R_s), electrical resistivity (*ρ*), carrier concentration (*N*), and Hall mobility (μ_H) of our ICO:H films on PET sheet.

the fact that the ICO:H film had a higher NIR transparency compared to that of the ITO film. This increased T_{av} in the NIR wavelength region was due to a lower *R* caused by the suitably low *N* of the ELI-*spc*-ICO:H film compared to that of ITO film[16,17]. For the ELI-*spc*-ICO:H film, the T_{av} in the absorption edge region slightly increased compared with that for the *a*-ICO:H and ITO films. This slight increase in T_{av} was due to the expansion of the optical bandgap. The difference in the positions of the absorption edges can also be attributed to the difference in *N*, namely, the blueshift due to the Burstein–Moss effect[47]. However, this is contrary to the Burstein–Moss shift for the ELI-*spc*-ICO:H film because the ITO film had the highest *N* and should therefore have the largest optical bandgap. A possible explanation for this is that the as-deposited ICO:H and ITO films were amorphous. Due to the disorder in the amorphous phase, optical transitions that usually do not occur due to both the top of the valence band and bottom of the conduction band being in parity with cubic bixbyite In_2O_3 structure could occur and thus lead to an optical bandgap similar to the fundamental gap[48–51]. Confirmation of such reduced disorder can be obtained by determining the electronic structure of the films by photoelectron spectroscopy (PES) measurements (discussed next).

Table 2 Survey of characteristics of In_2O_3 based TCO on PET sheet.

Dopant	Deposition technique (1)	Deposition (Annealing) temperature	Electrical resistivity (ρ) [Ωcm]	Carrier concentration (N) [cm^{-3}]	Hall mobility (μ_H) [cm^2/Vs]	Ref.
Ce	RPD	Unheated (ELI)	2.59×10^{-4}	1.92×10^{20}	126	This work
		Unheated (ELI + 100 °C)	2.13×10^{-4}	2.20×10^{20}	133	This work
W	RPD	Unheated	3.714×10^{-4}	2.72×10^{20}	61.7	57
	DC-MS	Unheated	4.41×10^{-4}	7.44×10^{20}	19.05	58
	DC-MS	Unheated (2)	4.46×10^{-4}	8.79×10^{20}	16.01	58
Sn	DC-MS	Unheated	6.0×10^{-4}	3.9×10^{20}	26.7	Commercially Available
	RPD	Unheated	1.58×10^{-4}	1.193×10^{21}	61.7	59
	DC-MS (3)	Unheated	4.6×10^{-4}	7.5×10^{20}	18.1	60
	DC-MS (4)	150 °C	5.4×10^{-4}	5.4×10^{20}	21.4	61
	DC-MS (4)	Unheated (5)	4.4×10^{-4}	3.3×10^{20}	43.5	61
Si	DC-MS	Unheated	1.588×10^{-3}	4.413×10^{20}	8.92	62
IZO	DC-MS (4)	150 °C	3.3×10^{-4}	4.0×10^{20}	47.1	61
non-doped	PLD	Unheated	4.1×10^{-4}	2.8×10^{20}	47	63

(1) Reactive plasma deposition (RPD), direct current magnetron sputtering (DC-MS), and pulse laser deposition (PLD), (2) Ar ion beam treated PET, (3) Thermionic emission (TE) enhanced DC-MS, (4) Reactive DC-MS, (5) Radio frequency (RF) bias to PET.

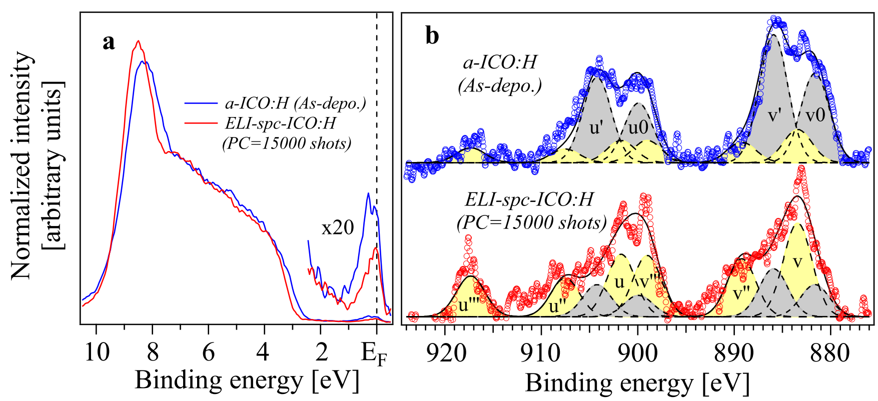

Fig. 4 Electronic structure of ICO:H films. **a** Valence band (VB) and **b** Ce 3*d* core spectra of the *a*-ICO:H film (nonlaser-irradiated) and fully crystalized ELI-*spc*-ICO:H film (*PC* = 15,000 shots).

Electronic structure

The electronic states of the *a*-ICO:H and ELI-*spc*-ICO:H films were investigated by using bulk-sensitive PES, i.e., hard-X-ray photoelectron spectroscopy (HAXPES) measurements. Figure 4a shows the valence band (VB) spectra of these films. The spectral intensity is normalized to each respective value at a binding energy of 6 eV. Note that the tail state at the valence band maximum (VBM) and the sharpness of the 9-eV peak in the VB spectra were affected by ELI. The VBM of the ELI-*spc*-ICO:H films was 2.88 eV (determined by linear extrapolation), and that of the *a*-ICO:H films was 2.66 eV. These features might be due to the laser irradiation-induced[52] enhancement in the crystallization of the films. Based on these results, we conclude that the increased *T* in the absorption edge by ELI (Fig. 3b) was driven by an increase in symmetry of the bixbyite structure due to the enhanced crystallization.

A weak peak near the Fermi energy (E_F of 0 eV in Fig. 4a) was also affected by ELI. The intensity of this effect was enhanced for the *a*-ICO:H films with a high N of 2.72×10^{20} cm^{-3} compared with the ELI-*spc*-ICO:H films with a low N of 1.91×10^{20} cm^{-3}. This peak is associated with occupied conduction-band states, and the intensity of this peak depends on the N of the film[53,54]. The phenomenon of N reduction upon crystallization of the a-ICO:H film was observed not only in laser crystallization but also in conventional heat-treatment crystallization[23,25]. For the IO:H films, Koida et al. explained that this phenomenon is due to the doubly charged donors (oxygen vacancies; $V_O^{\bullet\bullet}$) being exchanged by singly charged donors (interstitial H ($H_i^{\bullet}$) and/or to H being substituted for O ($H_O^{\bullet}$)) during the crystallization process that results in an approximately twofold reduction of N[23]. However, in the ICO:H films, possible carrier generation from Ce atoms must also be considered. Ce ions are well known to take on several electropositive charged states, such as Ce^{2+}, Ce^{3+}, and Ce^{4+}, in compounds. Note that in the +4 oxidation state (Ce^{4+} ion), Ce can act as an In-substituted (In^{3+}) dopant as a singly charged donor ($Ce_{In}^{\bullet}$). However, in the +3 oxidation state (Ce^{3+} ion), Ce can act as a neutral defect. Figure 4b shows the Ce 3d core spectra of the a-ICO:H and ELI-*spc*-ICO:H films. The Ce 3d spectra were fitted by 10 Voigt components after subtracting the background. All 10 features were observed in both films, indicating a mixture of the two oxidation states (+3 and +4). The observed peaks are attributed to Ce^{3+} and Ce^{4+}. These series of peaks are labeled "u" and "v", which are due to $3d_{3/2}$ and $3d_{5/2}$ spin–orbit states, respectively[55]. The four peaks labeled v_0, v′, u_0, and u′ (gray-shaded areas) are characteristic peaks of Ce^{3+}, whereas the peaks labeled v, v″, v‴, u, u″, and u‴ (yellow-shaded areas) are characteristic peaks of Ce^{4+}[55]. The ratio of the area intensities of the features attributed to Ce^{3+} (gray) and Ce^{4+} (yellow) was 27:73 for the ELI-*spc*-ICO:H films and 74:26 for the a-ICO:H films. This inversion ratio reveals that Ce^{4+} was formed preferentially after ELI application; thus, Ce atoms might be involved in the carrier generation in the polycrystalline phase rather than in the amorphous phase. However, the value of N raises doubt about the contribution of carriers from Ce donors. Further research that involves studying the effects of the precursor formation conditions, such as the H_2O pressure and O_2 gas flow rates, on the properties of ELI-*spc*-ICO:H films will provide further elucidation.

Conclusion

In summary, we systematically investigated the effect of the *PC* of the ELI technique on the solid-phase crystallization (*spc*) of a 150-nm-thick ICO:H film on a flexible PET sheet. With increasing *PC*, the film showed a large increase in μ_H from 42 to 126 cm^2/Vs with a large decrease in ρ (R_s) from 5.31×10^{-4} to 2.59×10^{-4} Ωcm (35.4 to 17.2 Ω/□). This change in μ_H was strongly correlated with the volume fractions of the amorphous and crystalline phases in the films. In the early stages of laser irradiation (*PC* < 2500 shots), crystallite nuclei were created by a rapid rise in the temperature. With increasing *PC*, these crystallites grew in addition to the nucleation of new crystallites. Grain growth by coalescence then progressed until the entire film was completely crystallized. At *PC* > 15,000 shots, the film was completely crystallized and consisted of slightly (111) oriented grains that had a maximum size of 2.4 µm. We also found that heat-assisted ELI was more effective for enhancing μ_H, and successfully obtained an ultrahigh μ_H of 133 cm^2/Vs compared with that of reported flexible TCO films and a low ρ (R_s) of 2.13×10^{-4} Ωcm (14.2 Ω/□) with exceptionally low absorptance in the near-UV-to-NIR part of the spectrum. This successful R_s value is much lower than that of commercially available 150-nm-thick ITO/PET sheets (R_s of 40 Ω/□). This study provides an exciting method for addressing the major challenge faced by existing flexible ITO films and replacing traditional ITO films, thus facilitating high-performance flexible optoelectronic devices.

Methods

Film deposition and crystallization

Reactive plasma deposition (RPD; Sumitomo Heavy Industries) without intentional heating was used to deposit 150-nm-thick a-ICO:H films onto 188-µm-thick PET sheets that had a 150-nm-thick a-SiO_2 coating. Here, the critical role of the a-SiO_2 layer was to adjust the thermal expansion between the ICO:H layer and the PET sheet and thus suppress the formation of cracks on the ICO:H films during laser irradiation[56]. We used ceramic tablets (Sumitomo Metal Mining) with In_2O_3 with a CeO_2 content of 2 wt.%. The deposition gases were Ar, O_2, and H_2O at a total pressure of 0.4 Pa. The flow ratio of O_2 to Ar was fixed at 31%, whereas the pressure of H_2O was ~1×10^{-4} Pa before deposition[25]. After deposition, the a-ICO:H films were irradiated with *PC*s of 2500, 5000, 10,000, 12,500, 15,000, and 30,000 shots by a KrF excimer laser (COMPex, Coherent Inc.) in an air atmosphere at room temperature or at 100 °C controlled by a hot plate. The two irradiation parameters, namely, the energy density and the frequency of the laser, were set at 40 mJ/cm^2 and 50 Hz, respectively[52].

Characterization

The microscopic morphology of the ICO:H film samples was evaluated using SIM (Hitachi FB-2100), and the crystallographic texture was characterized based on EBSD (JEOL JSM-7100F with EDAX Velocity Super). The N, μ_H, and ρ were determined by Hall effect measurements (Toyo Corporation, Resi Test 8300) at room temperature using the van der Pauw method. The optical properties were measured using a spectrophotometer (Hitachi, U-4000). The optical transmittance (T) and reflectance (R) spectra of the films in the wavelength range of 250–2500 nm were obtained using a spectrophotometer with an incident angle of 12°. The electronic states were estimated by using synchrotron HAXPES at beamline BL46XU at SPring-8 (photon energy, $h\nu = 7.939$ keV). The Ce charge state was determined using a laboratory HAXPES system, which consisted of monochromatized Cr Kα ($h\nu = 5.4$ keV). The E_F of the sample referred to that of the gold plate on the sample holder.

Acknowledgements

This research was supported by the Japan Society for the Promotion of Science, a Grant-in-Aid for Scientific Research (C) (Kakenhi Grant Number JP21K04148), and the AMADA Foundation (AF-2021242-C2). SIM measurements were conducted at the AIST Nano-Processing Facility supported by the "Nanotechnology Platform" of the Ministry of Education, Culture, Sports, Science and Technology (MEXT). The synchrotron radiation experiments were performed using beamline BL46XU at SPring-8 with the approval of the Japan Synchrotron Radiation Research Institute (JASRI) (Proposal No. 2020A1876). The authors express their sincere gratitude to Dr. Satoshi Yasuno of JASRI for their assistance with the HAXPES measurements.

Author details

[1]Advanced Manufacturing Research Institute, National Institute of Advanced Industrial Science and Technology (AIST), 1-1-1, Higashi, Tsukuba, Ibaraki 305-8565, Japan. [2]Research Institute for Energy Conservation, National Institute of Advanced Industrial Science and Technology (AIST), 1-1-1, Umezono, Tsukuba, Ibaraki 305-8568, Japan. [3]Department of Electronic and Photonic Systems Engineering, Kochi University of Technology, 185 Miyanokuchi, Tosayamada, Kami, Kochi 782-8502, Japan

Author contributions

J.N., T.K., and I.Y. conceived and designed the experiments. J.N., T.K., I.Y., and H.M. performed the experiments and the characterization of materials. T.N. and Y.K. contributed to the discussion of the results. T.T. supervised the project. J.N. wrote the manuscript, and all authors discussed the results and contributed to the manuscript.

Data availability

The data that support the findings of this study are available from the corresponding author upon reasonable request.

Competing interests

The authors declare no competing interests.

Publisher's note

Springer Nature remains neutral with regard to jurisdictional claims in published maps and institutional affiliations.

Received: 20 January 2022 Revised: 28 June 2022 Accepted: 30 June 2022. Published online: 16 September 2022

References

1. Klein, A. Transparent conducting oxides: electronic structure–property relationship from photoelectron spectroscopy with in situ sample preparation. *J. Am. Ceram. Soc.* **96**, 331–345 (2013).
2. Calnan, S. & Tiwari, A. N. High mobility transparent conducting oxides for thin film solar cells. *Thin Solid Films* **518**, 1839–1849 (2010).
3. Porch, A., Morgan, D. V., Perks, R. M., Jones, M. O. & Edwards, P. P. Electromagnetic absorption in transparent conducting films. *J. Appl. Phys.* **95**, 4734–4737 (2004).
4. Granqvist, C. G. & Hultåker, A. Transparent and conducting ITO films: new developments and applications. *Thin Solid Films* **411**, 1–5 (2002).
5. Lu, Q. et al. A review on encapsulation technology from organic light emitting diodes to organic and perovskite solar cells. *Adv. Funct. Mater.* **31**, 2100151 (2021).
6. Kaltenbrunner, M. et al. Flexible high power per-weight perovskite solar cells with chromium oxide-metal contacts for improved stability in air. *Nat. Mater.* **14**, 1032–1039 (2015).
7. Jung, H. S., Han, G. S., Park, N.-G. & Ko, M. J. Flexible perovskite solar cells. *Joule* **3**, 1850–1880 (2019).
8. Zhang, J., Zhang, W., Cheng, H.-M. & Silva, S. R. P. Critical review of recent progress of flexible perovskite solar cell. *Mater. Today* **39**, 66–88 (2020).
9. Dixon, S. C., Scanlon, D. O., Carmalt, C. J. & Parkin, I. P. n-Type doped transparent conducting binary oxides: an overview. *J. Mater. Chem. C.* **4**, 6946–6961 (2016).
10. Huang, K. et al. High-performance flexible perovskite solar cells via precise control of electron transport layer. *Adv. Energy Mater.* **9**, 1901419 (2019).
11. Jiang, Y. & Qi, Y. Metal halide perovskite-based flexible tandem solar cells: next-generation flexible photovoltaic technology. *Mater. Chem. Front.* **5**, 4833–4850 (2021).
12. Wang, C., Song, Z., Li, C., Zhao, D. & Yan, Y. Low-bandgap mixed tin-lead perovskites and their applications in all-perovskite tandem solar cells. *Adv. Funct. Mater.* **29**, 1808801 (2019).
13. Leijtens, T., Bush, K. A., Prasanna, R. & McGehee, M. D. Opportunities and challenges for tandem solar cells using metal halide perovskite semiconductors. *Nat. Energy* **3**, 828–838 (2018).
14. Yang, Z. et al. Stable low-bandgap Pb–Sn binary perovskites for tandem solar cells. *Adv. Mater.* **28**, 8990–8997 (2016).
15. Palmstrom, A. F. et al. Enabling flexible all-perovskite tandem solar cells. *Joule* **3**, 2193–2204 (2019).
16. Coutts, T. J., Young, D. L. & Li, X. Characterization of transparent conducting oxides. *MRS Bull.* **25**, 58–65 (2000).
17. Fujiwara, H. & Kondo, M., Effects of carrier concentration on the dielectric function of ZnO:Ga and In_2O_3:Sn studied by spectroscopic ellipsometry: analysis of free-carrier and band-edge absorption. *Phys. Rev. B* **71**, 075109 (2005).
18. Kothandaraman, R. K., Jiang, Y., Feurer, T., Tiwari, A. N. & Fu, F. Near-infrared-transparent perovskite solar cells and perovskite-based tandem photovoltaics. *Small Methods* **4**, 2000395 (2020).
19. Shigesato, Y., Takaki, S. & Haranoh, T. Electrical and structural properties of low resistivity tin-doped indium oxide films. *J. Appl. Phys.* **71**, 3356–3364 (1992).
20. Martins, R., Barquinha, P., Pimentel, A., Pereira, L. & Fortunato, E. Transport in high Mobility amorphous wide band gap indium zinc oxide films. *Phys. Status Solidi A* **202**, R95–R97 (2005).
21. Leenheer, A. J. et al. General mobility and carrier concentration relationship in transparent amorphous indium zinc oxide films. *Phys. Rev. B* **77**, 115215 (2008).
22. Koida, T., Fujiwara, H. & Kondo, M. Reduction of optical loss in hydrogenated amorphous silicon/crystalline silicon heterojunction solar cells by high-mobility hydrogen-doped In_2O_3 transparent conductive oxide. *Appl. Phys. Express* **1**, 041501 (2008).
23. Koida, T. et al. Hydrogen-doped In_2O_3 transparent conducting oxide films prepared by solid-phase crystallization method. *J. Appl. Phys.* **107**, 033514 (2010).
24. Kobayashi, E., Watabe, Y. & Yamamoto, T. High-mobility transparent conductive thin films of cerium-doped hydrogenated indium oxide. *Appl. Phys. Express* **8**, 015505 (2015).
25. Koida, T., Ueno, Y. & Shibata, H. In_2O_3-based transparent conducting oxide films with high electron mobility fabricated at low process temperatures. *Phys. Status Solidi A* **215**, 1700506 (2018).
26. Barraud, L. et al. Hydrogen-doped indium oxide/indium tin oxide bilayers for high-efficiency silicon heterojunction solar cells. *Sol. Energy Mater. Sol. Cells* **115**, 151–156 (2013).
27. Kobayashi, E., Watabe, Y., Yamamoto, T. & Yamada, Y. Cerium oxide and hydrogen co-doped indium oxide films for high-efficiency silicon heterojunction solar cells. *Sol. Energy Mater. Sol. Cells* **149**, 75–80 (2016).
28. Tutsch, L. et al. The sputter deposition of broadband transparent and highly conductive cerium and hydrogen co-doped indium oxide and its transfer to silicon heterojunction solar cells. *Prog. Photovolt. Res. Appl.* **29**, 835–845 (2021).
29. Jäger, T. et al. Improved open-circuit voltage in Cu(In,Ga)Se_2 solar cells with high work function transparent electrodes. *J. Appl. Phys.* **117**, 225303 (2015).
30. Steigert, A. et al. Sputtered Zn(O,S)/In_2O_3:H window layers for enhanced blue response of chalcopyrite solar cells. *Phys. Status Solidi RRL* **9**, 627–630 (2015).
31. Keller, J. et al. Direct comparison of atomic layer deposition and sputtering of In_2O_3:H used as transparent conductive oxide layer in $CuIn_{1-x}Ga_xSe_2$ thin film solar cells. *Sol. Energy Mater. Sol. Cells* **157**, 757–764 (2016).

32. Zhang, D., Soppe, W. & Schropp, R. E. I. Design of 4-terminal solar modules combining thin-film wide-bandgap top cells and c-Si bottom cells. *Energy Procedia* **77**, 500–507 (2015).
33. Fu, F. et al. Low-temperature-processed efficient semi-transparent planar perovskite solar cells for bifacial and tandem applications. *Nat. Commun*. **6**, 8932 (2015).
34. Yin, G., Steigert, A., Manley, P., Klenk, R. & Schmid, M., Enhanced absorption in tandem solar cells by applying hydrogenated In_2O_3 as electrode. *Appl. Phys. Lett*. **107**, 211901 (2015).
35. Schultes, M. et al. Sputtered transparent electrodes (IO:H and IZO) with low parasitic near-infrared absorption for perovskite–Cu(In,Ga)Se_2 tandem solar cells. *ACS Appl. Energy Mater.* **2**, 7823–7831 (2019).
36. Jiang, Y. et al. High-mobility In_2O_3:H electrodes for four-terminalperovskite/ Cu$InSe_2$ tandem solar cells. *ACS Nano* **14**, 7502–7512 (2020).
37. Moghadamzadeh, S. et al. In_2O_3:H-based hole-transport-layer-free tin/lead perovskite solar cells for efficient four-terminal all-perovskite tandem solar cells. *ACS Appl. Mater. Interfaces* **13**, 46488–46498 (2021).
38. Kitami, H., Miyashita, M., Sakemi, T., Aoki, Y. & Kato, T. Quantitative analysis of ionization rates of depositing particles in reactive plasma deposition using mass-energy analyzer and Langmuir probe. *Jpn. J. Appl. Phys*. **54**, 01AB05 (2015).
39. Macco, B. et al. On the solid phase crystallization of In_2O_3:H transparent conductive oxide films prepared by atomic layer deposition. *J. Appl. Phys*. **120**, 085314 (2016).
40. Scherg-Kurmes, H. et al. Optimization of the post-deposition annealing process of high-mobility In_2O_3:H for photovoltaic applications. *Thin Solid Films* **599**, 78–83 (2016).
41. Hosono, H., Kurita, M. & Kawazoe, H. Excimer laser crystallization of amorphous indium-tin-oxide and its application to fine patterning. *Jpn. J. Appl. Phys.* **37**, L1119–L1121 (1998).
42. Tsuchiya, T. et al. Characterization of tin-doped indium oxide films prepared by coating photolysis process. *Appl. Surf. Sci.* **197-198**, 512–515 (2002).
43. Chung, W., Thompson, M. O., Wickboldt, P., Toet, D. & Carey, P. G. Room temperature indium tin oxide by XeCl excimer laser annealing for flexible display. *Thin Solid Films* **460**, 291–294 (2004).
44. Nakajima, T., Tsuchiya, T., Ichihara, M., Nagai, H. & Kumagai, T. Epitaxial growth mechanism for perovskite oxide thin films under pulsed laser irradiation in chemical solution deposition process. *Chem. Mater*. **20**, 7344–7351 (2008).
45. Nakajima, T., Shinoda, K. & Tsuchiya, T. A universal value of effective annealing time for rapid oxide nucleation and growth under pulsed ultraviolet laser irradiation. *Phys. Chem. Chem. Phys.* **15**, 14384–14389 (2013).
46. Walsh, A. & Catlow, C. R. A. Structure, stability and work functions of the low index surfaces of pure indium oxide and Sn-doped indium oxide (ITO) from density functional theory. *J. Mater. Chem*. **20**, 10438–10444 (2010).
47. Hamberg, I. & Granqvist, C. G. Transparent and infrared-reflecting indium-tin-oxide films: quantitative modeling of the optical properties. *Appl. Opt*. **24**, 1815–1819 (1985).
48. Walsh, A. et al. Nature of the band gap of In_2O_3 revealed by first-principles calculations and X-ray spectroscopy. *Phys. Rev. Lett*. **100**, 167402 (2008).
49. Wardenga, H. F., Frischbier, M. V., Morales-Masis, M. & Klein, A. In situ Hall effect monitoring of vacuum annealing of In_2O_3:H thin films. *Materials* **8**, 561–574 (2015).
50. Aliano, A., Catellani, A. & Cicero, G., Characterization of amorphous In_2O_3: An ab initio molecular dynamics study. *Appl. Phys. Lett*. **99**, 211913 (2011).
51. Rosen, J. & Warschkow, O. Electronic structure of amorphous indium oxide transparent conductors. *Phys. Rev. B* **80**, 115215 (2009).
52. Nomoto, J., Matsui, H., Yamaguchi, I., Nakajima, T. & Tsuchiya, T. Origin of simultaneous enhancement of work function and carrier concentration in In_2O_3 films by excimer-laser irradiation. *Appl. Phys. Lett*. **118**, 101602 (2021).
53. Gassenbauer, Y. et al. Surface states, surface potentials, and segregation at surfaces of tin-doped In_2O_3. *Phys. Rev. B* **73**, 245312 (2006).
54. Körber, C. et al. Electronic structure of In_2O_3 and Sn-doped In_2O_3 by hard x-ray photoemission spectroscopy. *Phys. Rev. B* 81, 165207 (2010).
55. Bêche, E., Charvin, P., Perarnau, D., Abanades, S. & Flamant, G. Ce 3d XPS investigation of cerium oxides and mixed cerium oxide ($Ce_xTi_yO_z$). *Surf. Interface Anal.* **40**, 264–267 (2008).
56. Nomoto, J., Yamaguchi, I., Nakajima, T., Matsubayashi, Y. & Tsuchiya, T. Excimer laser annealing method for achieving low electrical resistivity and high work function in transparent conductive amorphous In_2O_3:Zn films on a polyethylene terephthalate substrate. *Thin Solid Films* **698**, 1378677 (2020).
57. Kim, J.-G., Na, S.-I. & Kim, H.-K. Flexible and transparent IWO films prepared by plasma arc ion plating for flexible perovskite solar cells. *AIP Advances* **8**, 105122 (2018).
58. Lee, J.-H. & Kim, H.-K. Flexible W-doped In_2O_3 films grown on ion beam treated polyethylene terephthalate substrate using roll to roll sputtering. *Mater. Sci. Semicond. Process.* **89**, 176–185 (2019).
59. Kim, J. H. et al. Flexible ITO films with atomically flat surfaces for high performance flexible perovskite solar cells. *Nanoscale* **10**, 20587–20598 (2018).
60. Lan, Y. F., Peng, W. C., Lo, Y. H. & He, J. L. Durability under mechanical bending of the indium tin oxide films deposited on polymer substrate by thermionically enhanced sputtering. *Org. Electron.* **11**, 670–676 (2010).
61. Miyazaki, Y., Maruyama, E., Jia, J., Machinaga, H. & Shigesato, Y. Indium oxide-based transparent conductive films deposited by reactive sputtering using alloy targets. *Jpn. J. Appl. Phys.* **56**, 045503 (2017).
62. Cho, D.-Y., Shin, Y.-H. & Kim, H.-K. Highly transparent Si-doped In_2O_3 films prepared on PET substrate using roll-to-roll sputtering. *Surf. Coat. Technol.* **259**, 109–112 (2014).
63. Dekkers, J. M., Rijnders, G. & Blank, D. H. A. Role of Sn doping in In_2O_3 thin films on polymer substrates by pulsed-laser deposition at room temperature. *Appl. Phys. Lett.* **88**, 151908 (2006).